Investigation of spalling in a 1D bar with damage models

Miguel Piteira Gomes
Advisor: Dr. Nicolas Moës

Thesis defense: Nantes, 26th of June 2013

Abstract

The aim of this study is the investigation of a fragmentation process that originates in the interior of materials as a result of the propagation of stress waves. This fragmentation process, known as spalling, is the result of uniaxial strain and high strain rate conditions, being thus associated to the molecular behaviour of the material.

The investigation will be conducted resorting to the development of a one-dimensional finite element code, integrating four damage laws. The objective of this work will be to retrieve the main characteristics of the spalling fracture, such as the determination of a spall strength value for a given material and the variation of the fracture size with the profile of the wave that travels internally.

Acknowledgments

I would like to thank to my advisor Professor Nicolas Moës for his guidance and enormous help during the course of this thesis.
I would also like to thank my family and friends for all the support given during a time which represented an enormous learning curve and was not always easy.

Table of contents

List of Figures

1. Introduction

1.1. Introductory notes

The purpose of this study is the simulation of a fracture phenomenon using a physically based model. The fracture type studied here is known as spalling and it is the result of high tensile waves travelling in the interior of a material body causing the opening of micro-voids or micro-cracks that will quickly evolve with time.

The first observations of spall fracture seemed to have been made in 1914 by Bertram Hopkinson, in experimental works relative to the wave propagation in solid media. His interest was linked to the detection of seismic waves, and to the investigation of acoustic frequencies and vibrations in acoustic experiments. He conducted his experiment based on the study of the relationship of the pressure with time when a projectile collides with a stiff surface.

Until the middle of the 1960's spalling was analysed as a discrete event and criteria was sought for its occurrence. The first intent to interpret the results as a gradual evolution of damage of conducted in 1943 by involving the stress rate by Tobolsky and Eyring and using the stress gradient in 1965 by I. C. Skidmore, in (Antoun, 2002).

The experiments conducted by Hopkinson in 1914 were the application of a simple theory based on the elastic propagation of stress pulses in a cylindrical rod when the amplitude of the pulse is high in comparison to the diameter of the bar. This is the necessary condition to guarantee that the wave will travel without distortion. A detailed explanation of the Hopkinson pressure bar is developed in (Kolsky, 1963).

In the present time a variety of innovative experimental techniques, measurements, and constitutive rate models are available for the study on spalling.

The experiments for the investigation of spalling are based on the generation of a stress pulse under uniaxial conditions. Spalling is characterised by the interaction of tensile waves developed at the highest rate possible for the material in question. Typical strain rates are of the order of 10^4 to $10^6\ /s$ for pulses with an amplitude usually of the order of 10^{-6} to $10^{-8}\ s$. The combination of uniaxial strain and high strain rates in experiments is a powerful procedure to analyse the microscopic processes that underlie and govern material strength, as stated in (Antoun, 2002).

The task to model this type of fracture is not easy as it deals with the microstructure of the materials. The approach presented in this study is based on the principles of continuum

mechanics, using a Lagrangian framework. A finite element model was developed based on the principle of virtual work.

In order to capture the spalling phenomenon four different damage laws were implemented in the constitutive equations. The first two damage models were known to be mesh dependent and were applied to prove the inability of these models to represent fracture. The two other models accounted with a regularization procedure, which consisted in the introduction a characteristic length dependent on the internal scales of the material sample.

1.2. Structure of the report

In the second chapter we begin by the definition of spalling. We then explain that in this type of dynamic fracture we are interested in the dynamic strength of the material and also on the size of the fractured zone for a set of impact loads. The existing experimental techniques are then presented where we analyse the data that we must take from the experiments in order to use as input in our numerical model to simulate the phenomenon. The discussion of the particularities of the two experimental techniques presented in then addressed.

We proceed with the formulation of our problem, to give the reader the idea of what we are trying to simulate. The formulation follows the theory of small strains of continuum mechanics and essays to give a first notion of where, when, and how damage will erupt due to spallation of the material body. The boundary conditions are presented as also the reflection process.

The second chapter finishes with a brief description of wave propagation using the method of characteristics. Here, we arrive to an important result that relates the density, wave speed, and impact velocity with the stresses generated at the bar. This relationship will be associated to one of the experimental techniques presented.

The third chapter begins with a mathematical formulation based on the principles of continuum damage mechanics to justify the introduction of d. It then presents the four models used in this study and describes how each one will act in its attempt to model the extension of damage across the domain.

Chapter four is dedicated to the numerical model implemented to determine the solution of the problem. In this chapter we begin with a brief description of the physical equations that govern the motion of stress propagation in solid media in order to describe the measures of stress and strain we intend to simulate.

We then move on to the finite element discretisation of our domain in space. This is achieved using a variational form designated by the principle of virtual work which consists in integrating the momentum conservation equation, coupled with the traction boundary conditions, multiplied

by a test function over the reference configuration. The terms inside the integral represent energy terms as the test functions stand for virtual displacements. This formulation is the approximation to the generalized momentum balance in strong form.

A description of the time integration of the variables at the nodes is then presented in section 4.3. Chapter four ends with some remarks of the stability of the implemented model

We continue by looking at the first result related to spalling, which will consist in the analysis of the velocity at the free-surface. This was said to be the main output of the plate-impact experiment as it is key to determine the spall strength of a material experimentally. Next, the measurement of the spalled zone is given with respect to a set of loads applied, close to the critical stress values and also for high loads. The typical damage profile for the four models is also presented. Then, we analyse the results for the energy dissipation, focusing on loads close to the threshold where crack-initiation arises. Finally, we study the mesh dependency of the four models. We end the chapter with a brief resume of the behavior of each model.

The chapter of the results includes the reflection of elastic waves at a free-surface, the analysis of free-surface velocity graphs, the results on the measurements of spalled layers and damaged profiles and the analysis of the energy dissipations, especially for loads very close to the threshold as the gradual loss of stiffness in an extremely small area can be very hard to capture.

Finally, we draw the conclusions based on the results obtained for our numerical model.

2. Spalling

2.1. Definition of Spalling

Spalling is a dynamic fracture phenomenon that occurs inside of a material body. It is closely associated to the propagation of stress waves in solid media, as it results from the interference of two strong plane decompression waves. It is characterized by uniaxial strain and high strain rates.

The loading in extremely short duration times leads to a type of fracture different than in other rupturing processes. During spalling millions of micro-cracks are generated in the interior of the material in a process designated by nucleation. For this reason the spalling strength of a material is closely associated to the theoretical strength of a material, that is, its strength in the absence of defects. As fracture occurs inside the body, it is a bulk material behaviour unaffected by surface defects, see (Antoun, 2002).

2.2. Experimental Techniques

In experimental tests, the stress waves imposed in the material can be very close to the threshold value and used to observe crack initiation, or on the other hand, be imposed at very high loads to produce immediate fragmentation from the absence of any damage and the analysis of the damaged layer.

The dynamic resistance to stress pulses is usually associated to the velocity pull-back in spalling experiments. From the graph of the free-surface velocity at the end of the sample we can directly measure the peak surface velocity, u_0, and the free-surface velocity before spalling, u_m, to calculate the tensile stress strength.

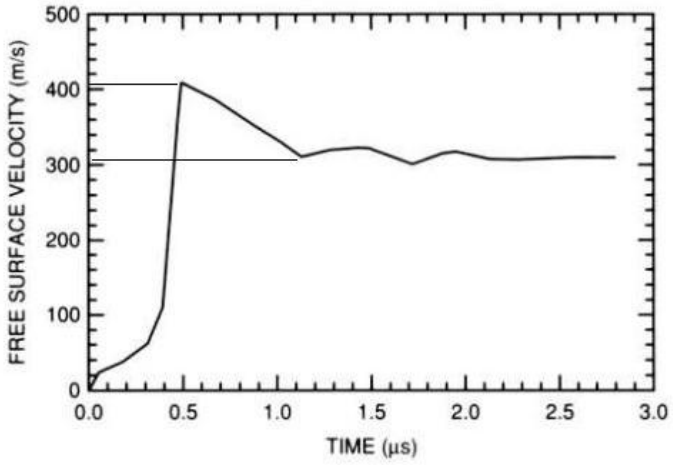

2.1 –Free-surface velocity for a aluminum target (image from (Antoun, 2002)).

The peak free-surface velocity, u_0, marks the end on the compression pulse, it is the velocity at the time when the reflection is half way and a tensile wave is about to appear at the boundary. The spalling strength is thus given by the linear approximation of the Riemann trajectories, explained in section 2.4, passing through the point of the peak and the point just before the pull-back as:

$$\sigma = \frac{1}{2}\rho_0 c_0 \Delta u_{fs}$$

The velocity pullback, Δu_{fs}, is the difference between u_0 and u_m. The approximation is accurate if the density and the wave speed in the material remain close to their initial values. As the tensile stress increases the relationship becomes less accurate.

The other important result from the experimental tests is the relationship between the spall diameter and the applied load.

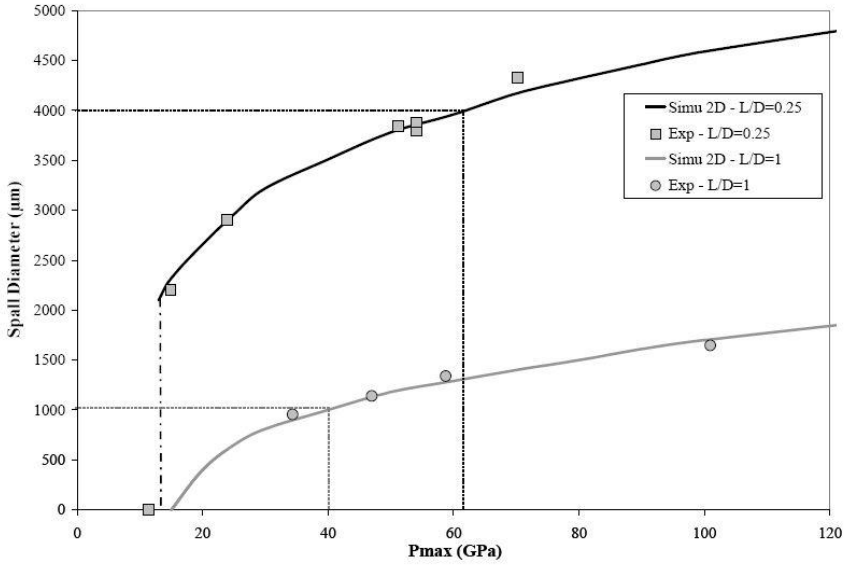

2.2 – Variation of the spall diameter with the initial impact load for an aluminum sample. (image from Rességuier, 2010a)

The experimental procedures used to produce shock loads will have an influence on the results. Amongst the different tests that can used to measure the dynamic fracture of a material we highlight two: the plate impact experiment and the laser beam radiation. Whilst the first technique is easier to be set in place, the laser beam radiation as the advantage of leaving less residual stresses on the material for its post analysis.

In both cases, the observation of the samples after a spalling experiment is followed by optical microscopy. As the fracture begins internally, the knowledge of the crystallographic structure of the material is important for an accurate measurement of the damage.

We discuss briefly some of the particularities of the two methods.

2.2.1. Plate impact experiments

Plate impact experiments are the most widely used configuration to measure the spall strength of a material. This technique uses shock-wave loading to study the behaviour of the material at very high strain rates. Figure 2.3 shows the typical configuration of the apparatus used in this technique:

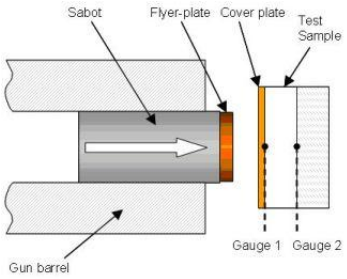

2.3 – Configuration of the plate-impact technique (image from cranfield.ac.uk)

The process is explained in (Kraus, 2009). We see in figure 2.3 that a flat flyer plate impacts a flat target plate over its surface simultaneously. The flyer plate can be driven by a gas gun, which is the common case in the western world, or it can be driven by an explosive load, a common case in Russia. The loading conditions considered in both cases consist in uniaxial strain, as the only non-vanishing strain component is the normal to the plane of the wave.

The experimental results are usually presented with the two initial parameter: the shock velocity (U_s) and the density of the two plates (ρ_0 and ρ_1). Then assuming that the shock is a steady wave it is possible to determine the stress applied at the target plate using the shock conservation equations:

Mass conservation: $$\rho_0 U_s = \rho_0 (U_s - u_p)$$

Momentum conservation: $$\sigma_{x,1} - \sigma_{x,0} = \rho_0 U_s u_p$$

Energy conservation: $$(\epsilon_1 - \epsilon_0)\rho_0 U_s = (\sigma_{x,1} - \sigma_{x,0})u_p - \frac{1}{2}\rho_0 U_s u_p^2$$

The variables u_p and ϵ represent respectively the particle velocity and the internal energy. The three conservation equations collectively are designated by the Rankine-Hugoniot jump conditions which describe the relationship between the two sides of a shock wave in a one dimensional flow. From these conditions we see that the amplitude and duration of the stress wave are thus controlled by the impact velocity and the thickness of the flyer plate. The magnitude of the stress waves generated inside the material body increase with the increase of impact velocity and the duration of the pulse is higher for larger target thickness. The relationship between plate thickness and the amplitude of the stress wave generated at the target plate is given by the dynamic impedance of the material.

2.2.2. Laser beam radiation

A more advance experimental technique in conducted using laser driven shock loading. The advantage of this method is in the time of pressure application. The shorter duration of the pulse irradiated by the laser source, usually ranging values of the ns-order compared to values of the μs-order for the plate impact, makes it less destructive than the more conventional techniques, as explained in (Rességuier, 2010a).

In this type of experiment the energy from the laser is absorbed by the front surface of the target. The depth of the deposition depends on the light absorption characteristic of the sample and on the laser beam. The short duration of the test causes local heating at constant volume, which leads to a stress increase. Since the front is a free-surface, it cannot sustain normal stresses, and it generates a rarefaction wave that travels along the material. A compression wave also forms due to energy dissipation, and spalling is the result of the interference of these two waves

Figure 2.4 shows schematically the intense irradiation of an absorbing target with a high power laser, leading to the vaporisation of a thin layer of material, transformed into a plasma cloud. What we see here is the response of a metallic foil to a laser shock above its melting pressure.

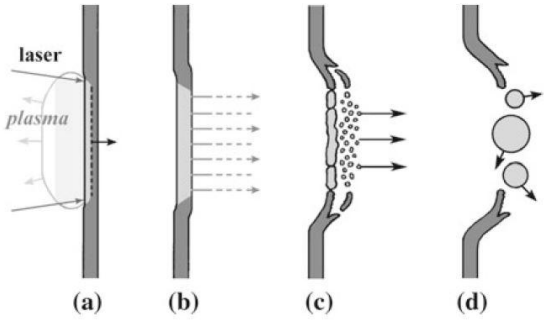

2.4 – Schematic representation from (Rességuier, 2009)

The author differentiates four distinct phases from the propagation of a compression wave induced by the expansion of the plasma cloud in (a); the reflection of the shock wave from the free-surface in (b); the ejection of micro-spall layers in (c); and remaining fragmentation of molten material in (d).

In figure 2.5 (a) it is clear the power of this experimental method from the images of the recovered-samples, marking clearly two distinct spalled areas of circular-like shape.

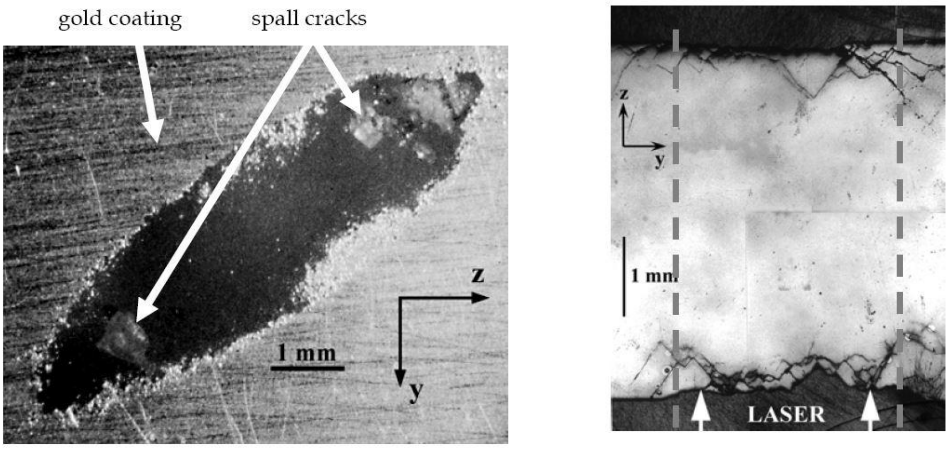

(a) (b)

2.5- Two recovered samples from (Rességuier, 2010a)

The tests shown in figure 2.5 correspond to two quartz samples. The first sample was charged with a laser shock of 42GPa on the x-direction. On the right we observe the results for a sample irradiated on the z-direction, leading to micro-cracks on the opposite extremity of the sample.

2.3. Description of my test case

The test case considered in this study is the failure resulting from the interaction of two strong decompression waves under uniaxial strain conditions, producing a region of tension inside the material body. This interaction results from the reflection of a compressive stress pulse at a free-surface. This is a type of failure associated to high strain rates where the stress pulse imposed has a duration commonly between the order of the microseconds.

The magnitude of the stresses imposed is much higher than the maximum strength measured using any other method, even for the strongest materials. This type of fracture can be the result of a bullet impact, a laser beam radiation, or an explosive load in contact with the surface of a bar. In our test case we consider a cylindrical bar subjected to a time dependent force at one extremity, in agreement to the plate-impact experiments. The uniaxial strain condition mentioned earlier is guaranteed by assuming at each plane the cross section of the rod will remain plane during the motion and the stress over it to be uniform. The diameter of the bar is taken small when compared to the amplitude of the pulse, in order to enforce the compressive wave to travel without distortion.

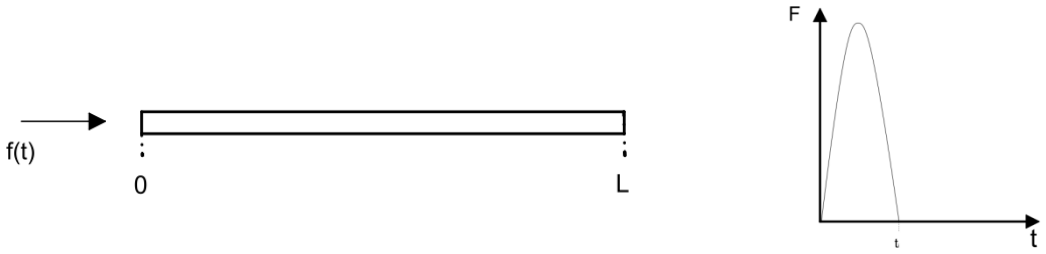

2.6- Test case model

The description of our model begins by considering a computation domain Ω bounded by Γ, where we can deduce the mathematical equations that allow us to describe our test case.

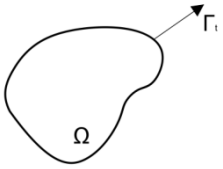

where $\Omega = [0, L]$.

2.7- Domain of our material body

The governing equation used is the wave equation for a rod of constant cross-section and modulus without a source:

$$\frac{\partial \sigma}{\partial x} = \rho \frac{\partial^2 u}{\partial t^2} \quad on\, \Omega \qquad \text{Eq. 2.1}$$

The stress is related to strain through a state law that will include damage in case of tension but not of compression. Taking E as the Hooke tensor, the state law will simply be the elastic law given by:

$$\sigma = E\varepsilon(1 - d) on\, \Omega$$

Here the scalar damage variable d shall vary between zero and one.

The damage energy release rate is defined from the strain energy density, E_D, by taking its derivative over the damage at constant stress:

$$Y = \frac{\partial E_D}{\partial D}\Big|_{\sigma = cst} = \frac{1}{2} E\varepsilon^2$$

The energy release shall be proportional to the stresses and the strains in our case.

The damage variable d will evolve accordingly to a function dependent of the energy release rate, which shall vary in each of the four damage models presented in chapter 3. This function will compare the damage energy release with one or two critical parameters depending on the damage model.

The boundary conditions in agreement to the experimental techniques, will require the prescription of tractions at one extremity of the rod during the time equivalent to the amplitude of the pulse that will travel along the bar. Hence the von Neumann conditions are given by:

$$\begin{cases}\sigma(0,t) = F(t) \\ \sigma(0,t) = 0\end{cases} on\ \Gamma$$

The rod will be considered to be at rest at the beginning of the computation yielding the following initial conditions given:

$$u(x,0) = 0 \quad x\epsilon\Omega$$

$$\dot{u}(x,0) = 0 \quad x\epsilon\Omega$$

The general solution of the partial differential equations described by Eq. 2.1, is given by the summation of two arbitrary functions, twice differentiable:

$$u(x,t) = f(x+ct) + g(x-ct) \qquad \text{Eq. 2.2}$$

In this equation the first function $f(x-ct)$ represents a wave travelling in the positive sense of the x-axis, and the second function $g(x+ct)$ represents a wave travelling in the opposite sense. Hence, for our specific case we can determine the stresses in elastic regime directly:

$$\varepsilon(x,t) = \frac{\partial u(x,t)}{\partial x} = f'(x-ct) + g'(x+ct) \qquad \text{Eq. 2. 3}$$

In our case, f represents the compression wave that travels along the bar and g does not exist. Then, when the compressive wave reaches the boundary we can see that the Neumann condition implies the equivalence of the derivatives of the general solution given above in Eq. 2.3.

$$\sigma(x,t) = E[f'(x-ct) + g'(x+ct)]$$

$$\sigma(L,t) = E[f'(x-ct) + g'(x+ct)] = 0 \Rightarrow f'(x-ct) = -g'(x+ct)$$

This result tells us that the Neuman condition can be analysed as the interaction, at that point, between the compression wave and a wave travelling in the opposite direction with the same amplitude and opposite sign as described by figure 2.6:

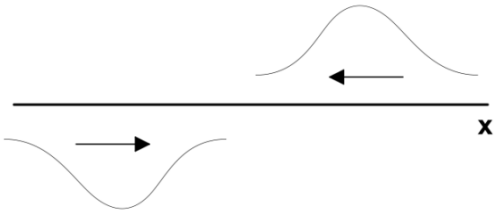

2.8 – Encounter of two waves travelling along the whole real line

The behaviour shall be considered elastic during the propagation of the compression pulse, and damage caused only by tensile stresses. As a result, damage shall start after reflection at the free-surface if the tensile wave reflected reaches the threshold of the material. The time instant at which damage begins is related to the magnitude and the amplitude of the applied stress.

$$\sigma(x,t) = -\sigma_M \sin\left(\frac{(x-ct)\pi}{c\tau_f}\right)$$

$$\sigma(x,t) = \sigma_M \sin\left(\frac{(x+ct)\pi}{c\tau_f}\right)$$

where σ_M is the magnitude of the stress wave and τ_f the duration of the pulse. This critical time, τ_c , is refered in spalling as the time at the spall plane. The spall plane is the location at which the reflected tensile wave first reaches the threshold value. Numerically we shall find this critical time by replacing x with $j * h$ and t by $i * dt$, for j nodes and i time steps, when the tensile wave reaches the stress limit. Notice the calculated time concerns only the distance travelled from the reflected boundary. In order to consider the propagation of the compression pulse we must account for the time up to the boundary. We do this by adding to τ_c the time it takes for the wave to travel along the entire bar, given by the bar length over the wave speed, L/c.

The location of the spall plane is also found numerically using the principle described above.

The results for the test case in chapter 5 follow a study of spalling in long bars conducted in (Diaz, 2002). In this paper the author consider mainly ceramic materials as they verify an elastic stress-strain relation, and their compressive strength is at least one order of magnitude higher than the tensile strength as noted by using diametric compression tests discs with uniform tensile stresses in the load plane.

2.4. Theory of characteristics

In this study we shall use the finite element method to investigate spalling in a one-dimensional bar. However, in this section we shall develop an alternative solution procedure designated by method of characteristics, as its mathematical procedure can be very useful for the understanding of the wave interaction.

Considering a flow field developed during the motion of a one-dimensional wave, we can identify characteristic lines as paths in the time-distance space where the partial differential equations governing the motion reduce to ordinary differential equations. In wave propagation these characteristic lines are particularly important because the wave motion occurs along these

directions. In a one-dimensional flow the waves propagate backward and forward in space giving rise to C- and C+ characteristics.

Inside the material the waves move at a sound speed defined, in Lagrangian coordinates as:

$$c = \frac{\rho}{\rho_0} c_0 = \frac{\rho}{\rho_0} \sqrt{\left(\frac{\partial \sigma}{\partial \rho}\right)_s}$$

where σ represents the stress in the direction of the wave propagation and the s index corresponds to the isentropic, ie., line of constant entropy, and the subscript 0 notes the reference configuration, as opposed to the actual configuration. As a result, c is the wave speed with respect to the material in motion. The characteristic lines $C+$ e $C-$ show the trajectories of the perturbations in the two directions for an isetropic flow. The slopes of these characteristic lines are given by:

$$\frac{\partial x}{\partial t} = c \quad on\ C_+$$

$$\frac{\partial x}{\partial t} = -c \quad on\ C_-$$

The variation of the state of the material along the charateristic lines in the time-distance plane is given by:

$$\frac{+du}{ds} + \frac{1}{\rho_0 c}\frac{d\sigma}{ds} = 0 \quad along\ \ C_+$$

$$\frac{-du}{ds} - \frac{1}{\rho_0 c}\frac{d\sigma}{ds} = 0 \quad along \quad C_-$$

where the integrals of these equations are the Riemann integrals:

$$u = u_0 - \int_{\sigma_0}^{\sigma} \frac{d\sigma}{\rho_0 c} \quad along\ C_+$$

$$-u = u_0 + \int_{\sigma_0}^{\sigma} \frac{d\sigma}{\rho_0 c} \quad along\ \ C_+$$

here u_0 and σ_0 are integral constants, see [Antoun,2002] for a more detailed explanation.

In the specific case dealt in this study we have the propagation of a simple wave. A simple wave can be described as a flow field in which all disturbances propagate in the same direction. The trajectory that describes the state variables in the $\sigma - u$ plane is known as the Riemann isentrope. The slope of the Riemann isentrope is the dynamic impedance of the material:

$$\frac{d\sigma}{du} = \pm \rho_0 c$$

We recall that the dynamic impedance of the material is what allows the relationship between plate thickness and the amplitude of the stress wave generated at the target plate in the plate-impact experiment.

3. Damage Modelling

The investigation of spalling requires the analysis of whether a meterial is damaged after the interference of stress waves at its interior. An important task is thus to create a constitutive law that represents the loss of mechanical properties if a given spall strength is reached. This loss is represented using a scalar parameter d introduced in the Hooke law.

This section begins with a mathematical formulation based on the principles of continuum damage mechanics to justify the introduction of d. As the study is one-dimensional most of the mathematical formulations became straightforward and easy to implement.

Subsequently we shall present the four models used in this study and describe how each one will act in its attempt to model the extension of damage across our domain.

3.1. Damage mechanics

The continuum damage mechanics approach aims to describe material discontinuities of the size of a representative volume element (RVE), as explained in [Lemaitre 1996]. Damage is thus defined for each RVE as the volume density of defects over the volume of the RVE.

The investigation of spalling, requires a constitutive relation using the mathematical formulation of continuum mechanics, but based on an observed description of the microscopic failure. Hence we introduce effective variables to make this relationship possible. We begin by defining the effective stress as a microscopic quantity:

$$\sigma_{eff} = E\varepsilon$$

and we shall relate the macroscopic stress to the effective variable as:

$$\sigma = (1 - D)\sigma_{eff}$$

Here the damage variable can be interpreted as the ratio between the surface density of micro-cracks and the cross sectional area:

$$D = \frac{A_D}{A_0}$$

In our case we shall treat compressive and tensile stresses differently, stating that damage will only occur due to tensile stresses resulting in:

$$\sigma = (1 - D)\langle\sigma_{eff}\rangle - \langle-\sigma_{eff}\rangle = E(1 - D)\langle\varepsilon\rangle - E\langle-\varepsilon\rangle$$

where $\langle\ \ \rangle$ represent the positive part of the tensor. The strain energy density is then defined as a function of the positive and negative parts of the stress:

$$E_D = \frac{1}{2}\left[\frac{\langle\sigma\rangle^2}{E(1-D)} + \frac{\langle-\sigma\rangle^2}{E}\right]$$

Finally we introduce the energy density release rate variable Y, given as the derivative of the strain energy density over the damage. As damage is a state variable, the energy density release rate is responsible for the thermodynamic closure of the model.

$$Y = \left.\frac{\partial E_D}{\partial D}\right|_{\sigma=cst} = \frac{\langle\sigma\rangle^2}{2E(1-D)}$$

The energy release rate is what will drive the damage in our models. It is defined such that its product with the damage rate represents the dissipated power during the damage process. We define the energy dissipation as:

$$Diss = \int_0^L \int_0^T Y\dot{d}\ dt.dx$$

The damage rate will evolve differently for each damage model, but it will always depend on two material constants and the difference between either the damage energy release function and fracture, the case of models 1 and 3, or it will depend on the difference between the damage release function and the damage variable D.

3.2. Damage models

As referred in (Allix, 2002) it is a well known fact that classical damage models are unable to describe facture correctly. One of the objectives of this study was to arrive to this conclusion. The numerical simulation of failure induced by strain softening suffers from mesh dependency, conditioning the localization of the fracture to a single element. This phenomenon is known as spurious localization.

A way of avoiding such numerical difficulties is to use localization limiters. This is conducted by introducing a length scale implicitly in the constitutive model to eliminate the sensibility of the mesh to this malice. This regularization procedure is material dependent, and the length scale is related to the internal scales of the material.

The four models chosen will behave very differently in their attempt to investigate spalling at the bar. Hence we shall briefly present their equations and using the mechanical parameters in table 3.1.

Table 3-1 – Mechanical and geometrical properties of the sample

E	ρ	L	diameter
360 GPa	3840 kg/m^3	0.1 m	0.04 m

We shall now present our two classical models, and two models with a delay effect that attempt to overcome the deficiencies of the classical models.

3.2.1. Damage model 1

The first damage model is based on the classic approach and uses only one parameter to guide the energy density release function. The critical energy release rate, Yc, will be responsible for the initiation of damage.

$$f(Y) = \frac{\sqrt{Y}}{\sqrt{Y_c}}$$

The evolution of damage is conducted by the damage rate as explained above and in this model according to the following law:

$$\dot{d} = \frac{1}{\tau_c}(a\langle f(Y) - 1\rangle_+)$$

We see here that the damage rate depends on the difference between the damage energy release function and fracture.

The damage profile is then traced, in figure 1, for the conditions explained above.

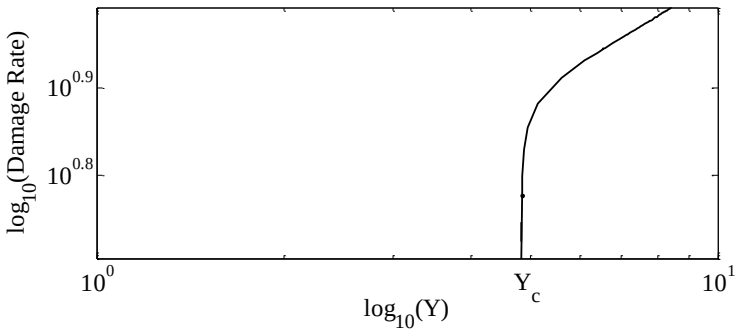

3.1-Damage-rate law for the damage model 1

From the figure 3.1 we can see that no ceiling is set on the damage-rate evolution. Damage will initiate at a critical value, Y_c, and the damage rate will tend quickly to very large values.

3.2.2. Damage model 2

In the second damage model, a new parameter is introduced. The formulation of the elastic yield function will include the same parameter Y_c as in the previous model, responsible for the initiation of damage, and it shall also count with a parameter Y_0, that will define how fast the damage rate will tend to infinity.

$$f(Y) = \frac{\sqrt{Y} - \sqrt{Y_0}}{\sqrt{Y_c} - \sqrt{Y_0}}$$

In the second model the damage rate law reads:

$$\dot{d} = \frac{1}{\tau_c}(a\langle f(Y) - d\rangle_+)$$

The damage rate will vary between the damage energy release and the previous value of damage.

The damage-rate profile for the second model is illustrated below:

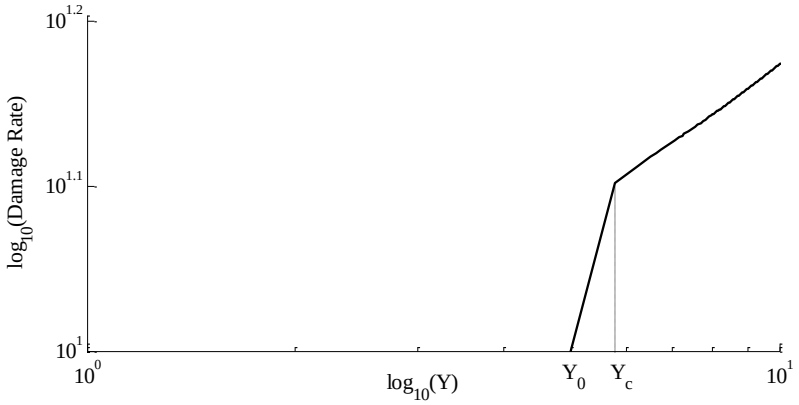

3.2 – Damage-rate variation for an impact load equal or above the critical tensile stress

In this model the damage rate will evolve linearly from a critical value Y_0, until Y_c and consequently so will the damage. The introduction of the parameter Y_0 should lead to a smoother rise of damage in comparison to the previous model.

3.2.3. Damage model 3

The third damage model uses the same parameter Y_c to start the damage as in model 1.

$$f(Y) = \frac{\sqrt{Y}}{\sqrt{Y_c}}$$

However in this model we introduce a length scale to condition the damage rate and prevent spurious localization. The damage-rate law reads:

$$\dot{d} = \frac{1}{\tau_c}\left(1 - e^{-a\langle f(Y)-1\rangle_+}\right)$$

In (Deü, 1997) and (Suffis, 2003) the authors introduce constants a and τ_c as empirical constants material dependent to get the fourth model. However, for the case of model 3 here discussed, we can see that fracture will only take place for critical stresses in the numerical

algorithm, if τ_c is equal to the time increment, that is the time it takes for the wave to travel through an element. As we are using the difference between $f(Y)$ and 1 in the exponential power, we see that for stresses close to the threshold the energy release function will be high enough for the exponential of a negative large number to be zero, as a is a positive scale factor. Hence, as the damage rate will quickly reach $1/\tau_c$, the only way to reproduce the fragmentation of our sample for stress waves very close to the critical stress is to play with these two parameters to get a combination equivalent to having $a = 1$ and τ_c equal to the time increment.

The variation of the damage rate with the energy release rate for this model is presented below:

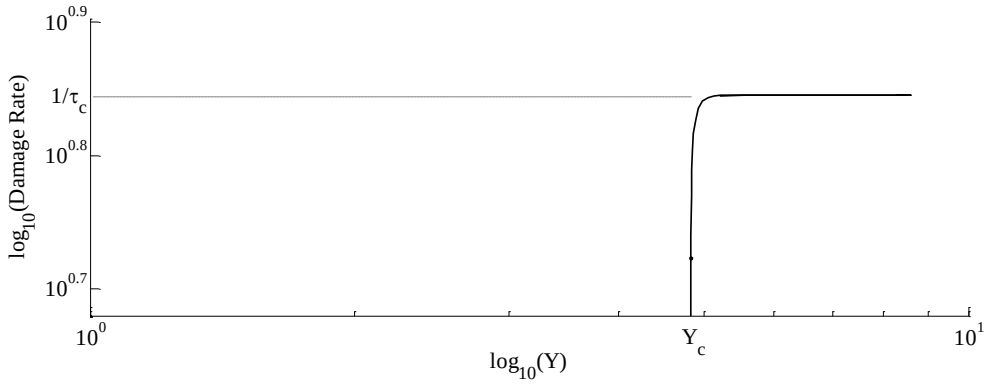

3.3 – Damage-rate profile for model 3.

Here we can observe that damage will initiate when the tensile stress reaches the critical value, during reflection on our particular case, and the damage rate shall be constant while the value of the stress remains above the critical value. The value of Y_c is associated to the critical stress, which we associate to the spall strength. Hence we can already expect misbehavior for loads close to the threshold.

3.2.4. Damage model 4

The fourth model will have two critical parameters, a parameter Y_c responsible for starting the damage, and a parameter Y_c' related to the fracture, that is, to the value of damage equal to 1. The first parameter is associated to a lower tensile strength, and the second associated to the spall strength, as the value required to initiate fracture.

$$f(Y) = \frac{\sqrt{Y} - \sqrt{Y_c}}{\sqrt{Y_c'} - \sqrt{Y_c}}$$

The damage-rate law for this model reads:

$$\dot{d} = \frac{1}{\tau_c}\left(1 - e^{a\langle f(Y) - d\rangle_+}\right)$$

The advantage of having this new parameter, Y_c' , in the damage yield function, with respect to model 3, is that we can guarantee that our material body will fracture for stress wave values very close to the critical stress, without adapting any material parameters to numerical implementations.

The damage profile for model 4 is presented below:

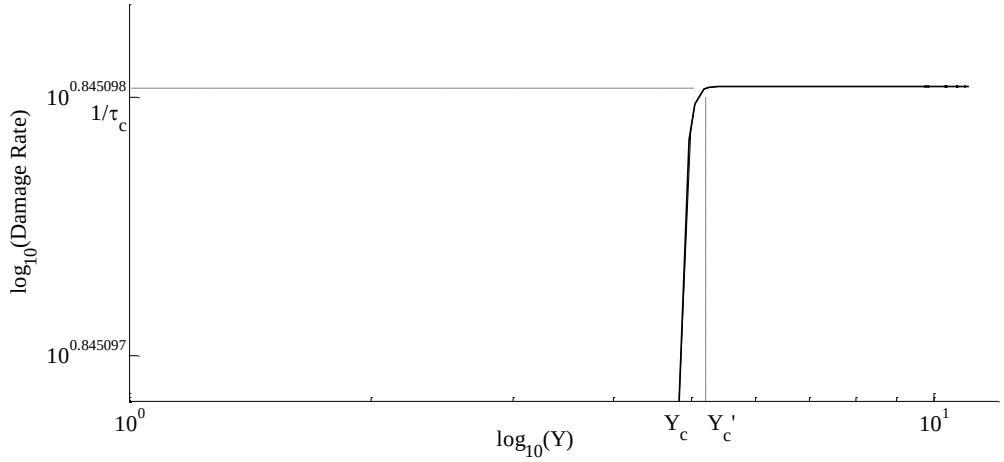

3.4 – Damage-rate law for model 4.

4. Numerical Model

4.1. Physical description

The formulation of a numerical model for the resolution of a physical problem comprehends the resolution of an ensemble of governing equations. Hence, we begin with the fundamental hypothesis of solid mechanics integrated in the continuum mechanics theory. We followed the books (Belytschko, 2000), (Holzapfel, 2000) and (Bonet, 1997), in the elaboration of this chapter. Our aim, is to observe the particles that make part of our material domain as a continuum body, part of the Euclidian space. This assumption assumes that a continuum particle represents the collective behavior of all the molecules that are part of that particle.

We thus begin with a brief description of the physical equation which describes the problem studied, moving on to a weak formulation of these equations in order to establish the finite element method used to determine the unknowns.

We can proceed synthetically to the description of our problem using a Lagrangian structure, popular in solid mechanics problems. Figure 4.1 describes the configuration and motion of a continuum body which occupies a domain Ω with boundary Γ, showing also a set of admissible lines of interwoven discontinuities in the notation.

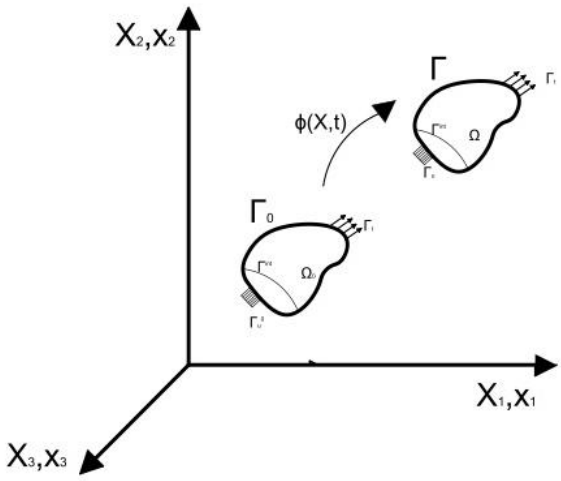

4.1 – Configuration and motion of a continuum body

The governing equations that describe the mechanical behaviour of a continuum body are namely mass conservation:

$$\rho J = \rho_0$$

where J is the jacobian between the current and reference configurations. In one-dimensional mappings we have that $J\big(x(X)\big) = \partial x/\partial X$.

The measure of stress always requires some intuition as it something that we cannot see. It is easy to measure a deformation caused by a stress but to visualize a measure of stress is not possible to the eye. In the total Lagrangian description, the nominal stress is used for the equation of linear momentum conservation instead of the usual Cauchy stress, σ,to facilitate the weak formulation later on.

$$\frac{\partial P_{ji}}{\partial X_j} + \rho_0 b_i = \rho_0 \ddot{u}_i$$

The nominal stress, P, does not refer the total force applied to a section T to the current area but to the initial undeformed area A_0.

$$\sigma = \frac{T}{A}, \qquad P = \frac{T}{A_0}$$

The angular momentum conservation that indicates the symmetry of the stress tensor is also given for our description as:

$$F_{ij} P_{jk} = F_{kj} P_{ji}$$

Although the energy conservation equation shall not be needed to solve in our model, it is presented here for the purely mechanical problem as the internal work, on the left hand side, equal to the product of the rate of deformation with the nominal stress:

$$\rho_0 \dot{w}^{int} = \dot{F} P - q_{x,X} + \rho_0 s$$

$$\rho_0 \dot{w}^{int} = \dot{F} P$$

The constitutive equation depends on the $F^T F$ and not simply on the deformation tensor alone, as it would not annul itself for rigid body motion. The nominal stress is incorporated into the equation so it satisfies the conservation of angular momentum and we introduce a scalar variable d to represent the damage of the material. The evolution of this damage variable shall be discussed in the next section.

$$P = S F^T (1 - d)$$

Finally, the equation that relates the strains with the displacements, in our Lagrangian Framework, is given:

$$E_{ij} = \frac{1}{2}\left(F_{ki} F_{kj} - \delta_{ij}\right)$$

Here, the green stain tensor, E, gives the change in the length square of the material vector d$\mathbf{X}$, where d$\mathbf{X}$ pertains to the undeformed configuration. Therefore, the Green strain measures the

difference of the length square of an infinitesimal segment in the current configuration to the reference configuration.

The advantage of using a Lagrangian Framework is that all the equations are calculated in the same material points. The dependent variables are functions of the material coordinates and time. The weak formulation involves the integrals over the reference configuration and the derivatives are taken with respect to the material coordinates.

The boundary conditions described in equation 4.1 indicate that across the boundary we must prescribe tractions or displacements. We can also prescribe velocities as boundary conditions and relate it to the displacements using time differentiation.

$$n_j^0 P_{ij} = \bar{t}_i^0 \quad \text{on } \Gamma_{t_i}^0,\ u_i = \bar{u}_i \text{ on } \Gamma_{u_i}^0$$
$$\Gamma_{t_i}^0 \bigcup \Gamma_{u_i}^0 = \Gamma^0 \qquad \Gamma_{t_i}^0 \bigcap \Gamma_{u_i}^0 = 0 \text{ for } i = 1 \text{ to } n_s \qquad \text{Eq. 4.1}$$

The initial conditions may be applied to the velocities and stresses or otherwise to the velocities and displacements. Although the first set is more adequate as the initial displacement of a body may be hard to determine, the initial stresses, known as residual stresses, may frequently be estimated using equilibrium equations, thus becoming redundant its prescription.

$$P(x, 0) = P_0(x)$$

$$u(x, 0) = u_0(x)$$

4.2. Finite element discretisation

The pivotal equation in the nonlinear finite elements approach comes from momentum conservation. This equation is a form of Newton's second law of motion that relates the forces acting on a body with its acceleration. However, this equation cannot be directly discretized by the finite element method. In order to do so, it is necessary to obtain a variational from. The principal of virtual work is what establishes this correlation between a strong form, composed by the momentum equation coupled with the traction boundary conditions, and a weak form, composed by a balance of virtual energies that will yield an approximate to the generalized momentum balance from the strong form.

The development of the weak formulation begins with the definition of a test function $\delta u(X, t)$ that we can use to transform the terms of the momentum equation into energy terms. These test functions represent virtual displacements and will have to meet the displacement boundary conditions and be smooth enough so that all the derivatives in the momentum equation are well defined.

The weak form is obtained from the product of the momentum equation with the test function, integrating over the reference configuration:

$$\int_{X_a}^{X_b} \delta u\left[(A_0 P)_{,X} + \rho_0 A_0 b - \rho_0 A_0 \ddot{u}\right] dX = 0$$

By transforming the first term of the equation using the derivative of the product we can eliminate the derivative of the nominal stress:

$$\int_{X_a}^{X_b} \delta u (A_0 P)_{,X} dX = \int_{X_a}^{X_b} \left[(\delta u A_0 P)_{,X} - \delta u_{,X} A_0 P\right] dX$$

By applying the Gauss theorem we can express the terms of the right hand side of the equation as a boundary integral:

$$\int_{X_a}^{X_b} \delta u (A_0 P)_{,X} dX = -\int_{X_a}^{X_b} \delta u_{,X} (A_0 P)\, dX + (\delta u A_0 n^0 P)|_\Gamma$$

$$= -\int_{X_a}^{X_b} \delta u_{,X} (A_0 P)\, dX + (\delta u A_0 \bar{t}_x^0)|_\Gamma$$

Here, the second term comes from the fact that the test function $\delta u(X,t)$ vanishes at the prescribed displacement boundary, on the complementary conditions on the boundaries and on the traction boundary conditions. Substituting this expression for the first term of equation 1 we obtain:

$$\int_{X_a}^{X_b} [\delta u_{,X} A_0 P - \delta u(\rho_0 A_0 b - \rho_0 A_0 \ddot{u})]\, dX - (\delta u A_0 \bar{t}_x^0)|_\Gamma = 0$$

The last term will vanish on the equation above, from the internal continuity condition. As the first term on the right we can see that it is simply the traction boundary condition as:

$$\delta u_i = 0 \text{ on } \Gamma_{u_i}^0 \text{ and } \Gamma_{t_i}^0 = \Gamma_0 - \Gamma_{u_i}^0$$

Hence,

$$\int_{\Omega_0} \frac{\partial}{\partial X_j}(\delta u_i P_{ji}) d\Omega_0 = \int_{\Gamma_0} \delta u_i n_j^0 P_{ji} d\Gamma_0 = \sum_{i=1}^{n_{SD}} \int_{\Gamma_{\text{tj}}^0} \delta u_i\, \bar{t}_i^0\, d\Gamma_0$$

where the last equality comes from the strong form. We also notice from the definition of the deformation gradient that:

$$F_{ij} = \delta\left(\frac{\partial u_i}{\partial X_j}\right)$$

Rearraging all these equations we can finally write the weak form of the momentum equation, traction boundary conditions and interior continuity conditions. The weak form is named also

principle of virtual work because each term of this equation is a virtual work increment. The second and forth terms of the equation represent the body forces and prescribed tractions, which we designate by virtual external work, as they result from external forces:

$$\delta W^{ext} = \int_{X_a}^{X_b} \delta u \rho_0 b A_0 \, dX + (\delta u A_0 \bar{t}_x^0)|_{\Gamma_t}$$

The first term corresponds to the virtual internal work as it is derived from the stresses inside the material, $\delta w^{int} = \delta u_{,X} P/\rho_0$ consistent with the energy conservation derived in the previous section:

$$\delta W^{int} = \int_{X_a}^{X_b} \delta u_{,X} P A_0 \, dX = \int_{X_a}^{X_b} \delta F P A_0 \, dX$$

The term $\rho_0 A_0 \ddot{u}$ is considered a body force acting in the direction opposite to the acceleration, as in corresponds to a virtual internal work

$$\delta W^{inert} = \int_{X_a}^{X_b} \delta u \rho_0 A_0 \ddot{u} \, dX$$

The principle of virtual work can then be written involving these three contributions as:

$$\delta W(\delta u, u) \equiv \delta W^{int} - \delta W^{ext} + \delta W^{inert} = 0$$

The finite element method can now be applied by dividing the domain interval [Xa,Xb] in a finite number of elements and choosing an appropriate test function to interpolate the value of the function over each element. We denote de nodes by $X_I, I = 1 \; to \; n$ and the elements by ${X_I}^e, I = 1 \; to \; n - 1$. The finite element trial function u(X,t) is given the by:

$$u(X,t) = \sum_{I=1}^{n} N_I(X) \, u_I(t)$$

where $N_I(X)$ are the shape functions relative to the spatial discretisation and $u_I(t)$ the displacement variables.

From the principal of virtual work we can establish the following relationships for the forces:

$$\delta W^{int} = \sum_{I=1}^{n} \delta u_I f_I^{int} = \delta \mathbf{u}^T \mathbf{f}^{int}$$

$$\delta W^{ext} = \sum_{I=1}^{n} \delta u_I f_I^{ext} = \delta \mathbf{u}^T \mathbf{f}^{ext}$$

$$\delta W^{inert} = \sum_{I=1}^{n} \delta u_I f_I^{inert} = \delta \mathbf{u}^T \mathbf{f}^{inert}$$

$$\delta \mathbf{u}^T = \left[\delta u_1 \; \delta u_2 \; \ldots \; \delta u_{n_N}\right] \quad \mathbf{f}^T = [f_1 \; f_2 \; \ldots \; f_{n_N}]$$

Here, the internal nodal forces correspond to the stress waves travelling in the interior of the material, the external applied loads to the initial boundary condition we impose and the inertia term to the accelerations.

Defining the internal nodal forces in terms of nominal stress we have:

$$\delta W^{int} \equiv \sum_{I=1}^{n_N} \delta u_I f_I^{int} = \int_{X_a}^{X_b} \delta u_{,X} A_0 P \, dX = \sum_I \delta u_I \int_{X_a}^{X_b} N_{I,X} A_0 P \, dX$$

Thus yielding the value for the internal forces

$$f_I^{int} = \int_{X_a}^{X_b} N_{I,X} A_0 P \, dX$$

The external forces are derived similarly from the principle of virtual work as:

$$\delta W^{ext} = \sum_I^N \delta u_I f_I^{ext} = \int_{X_a}^{X_b} \delta u \rho_0 b A_0 \, dX + (\delta u A_0 \bar{t}_x^0)|_{\Gamma_t}$$

$$= \sum_I^N \delta u_I \left\{ \int_{X_a}^{X_b} N_I \rho_0 b A_0 dX + (N_I A_0 \bar{t}_x^0)|_{\Gamma_t} \right\}$$

Giving:

$$f_I^{ext} = \int_{X_a}^{X_b} N_I \rho_0 b A_0 dX + (N_I A_0 \bar{t}_x^0)|_{\Gamma_t}$$

The inertial forces derived as:

$$\delta W^{inert} = \sum_I^n \delta u_I f_I^{inert} = \int_{X_a}^{X_b} \delta u \rho_0 \ddot{u} A_0 dX$$

Rearranging for the finite element approximation we have:

$$\sum_I^n \delta u_I f_I^{inert} = \sum_I \delta u_I \int_{X_a}^{X_b} \rho_0 N_I \sum_J N_J \ddot{u}_J A_0 dX$$

The inertial nodal force is usual expressed as a product of the mass times acceleration. Hence we separate the acceleration term and define the mass matrix as:

$$M_{IJ} = \int_{X_a}^{X_b} \rho_0 N_I N_J A_0 dX$$

And we define the inertial forces as:

$$f_I^{inert} = \sum_J M_{IJ} a_J$$

with $a_J = \ddot{u}_J$.

We then find the generalized momentum balance as:

$$\mathbf{Ma} = \mathbf{f}^{\text{ext}} - \mathbf{f}^{\text{int}} \qquad \text{Eq. 4.2}$$

for the domain at each iteration in time.

4.3. Time-integration

The momentum equation given by equation 4.2 is a differential equation in time. Its solution will be sought with an explicit scheme as it is a highly nonlinear problem.

We begin our time-integration algorithm by initializing our variables for the displacements, velocities and accelerations at the nodes. The two first fields will be initiated at zero at each increment in time. The acceleration vector will be initialized with the application of the initial condition which is given by the force history applied at the left node over the mass at this node.

$$a_{N1}^{t-1} = \frac{F(t)}{m_1}$$

All the other nodes will assume a zero value. We then proceed with by determining the predicted displacements and velocities as:

$$\begin{cases} v^t = v^{t-1} + a^{t-1} \dfrac{\Delta t}{2} \\ u^t = u^{t-1} + \Delta t . v^t \end{cases}$$

We proceed to calculate the strains at each time iteration as the difference between the displacements at the two nodes over the size of the element.

$$\varepsilon^t = \frac{u_{N2}^t - u_{N1}^t}{h}$$

If the value for the strain is positive we compute the damage release rate and its function according to the equations in chapter 3 for each model. The damage rate and consequently the damage evolution law are also calculated at each time iteration for the given damage model.

The computation of the stresses follows the constitutive equation and is given at each element by:

$$\sigma^t = E(1-d)\varepsilon^t$$

We then calculate the accelerations for the middle nodes of the bar based on the stresses as:

$$a^t = \frac{A.\sigma_{e2}^t - A.\sigma_{e2}^t}{m_{N1}}$$

where m_{N1} is the mass of a middle node. The mass of the nodes at the extremities is half the mass of the interior nodes because they have the contribution of only one element. The mesh size is uniform, that is, the element size is constant.

In the nodes at the ends of the bar the acceleration assumes the traction boundary condition as mentioned above. We now update the acceleration value of the left node to account with the pulse applied:

$$a_{N1}^t = \frac{A.\sigma^t + F^t}{m_{N1}}$$

And we define the free-surface boundary condition at the right end of the bar as:

$$a_{NN}^t = \frac{0 - A.\sigma^t}{m_{NN}}$$

We see that the von Neumann homogenous boundary condition is thus imposed in a weak sense making this boundary condition satisfied only in an approximated way.

The velocities and displacements are then updated to complete the iteration cycle.

$$\begin{cases} v^t = v^t + a * \dfrac{\Delta t}{2} \\ u^t = u^t \end{cases}$$

4.4. Stability of the model

The explicit dynamics algorithm is easily implemented in a finite element code. The explicit time integration is robust in the sense that it seldom aborts due to a failure of the numeric algorithm.

The disadvantage of explicit method lies in the stability condition imposed. If the time increment surpasses a critical value the solution can diverge without border and will be wrong in any case, see (Bathe, 1996).

The critical time depends on the mesh and the material proprieties. For the scheme here presented the critical time is given by the time it takes for a wave to travel over an element:

$$t_c = \frac{h}{c}$$

Where c is the velocity of propagation of the wave inside the material defined by $c = \sqrt{E/\rho}$ and h is the element size. Hence we can see that the critical time decreases when we refine the mesh or increase the stiffness of the material. If the time increment is above the critical value the solution will explode due to a numerical instability.

A numerical instability is related to the numerical solution of the problem, as opposed to a physical instability which is related to the solution of the model. The numerical instabilities come from the discretisation of the equations of the model, whereas the physical instabilities are independent of the numeric discretisation and refer to whether the physics of the model is described.

The explicit schemes have great difficulties in dealing with strong discontinuities in traction boundary condition, which is imposed weakly as mentioned in section 4.3. In order to reduce as much as possible the noise generated due to the application of the external forces, a half-sine pulse was chosen as the load input instead of the classical ramp pulse used in plate-impact experiments or triangular shaped loads in explosive ones.

5. Results

The results presented in this report are based on the case-study developed in chapter 2, involving the reflection of a compressive pulse into a tensile one at a free-surface, and generating the internal fragmentation of the material when this tensile stress reaches a spall threshold. Numerically, this means that it is very important to control the reflection process and make sure the time increment is sufficiently small to yield a smooth motion transition during this process. This task is not so elementary when treating the samples extracted from the new laser-induced loads, applied over nanoseconds in the surface of a sample. As explained in section 4.4, the critical time step is related to the time it takes for a wave to travel over an element, and is thus intrinsically related to the mesh size. If we want to obtain a time increment of the order of 10^{-10}, our mesh size will have to be of the order of 10^{-7} as the samples are usually several mm long. This leads to very high calculation times above the abilities of our code programmed using MATLab. Consequently, the numerical simulations were based upon the impact test and not the laser-induced discussed in section 2.2, even though the latest experiments of De Resseguier show impressive details of the nucleation process during fragmentation, which provide a good source for the comparison of the spalled layer.

The study followed was on spalling in long bars conducted in (Diaz, 2005). The mechanical parameters of the ceramic material Al_2O_3 99.5% chosen in this study are describe in table 5.1.

Table 5-1 – Material properties and geometry of the sample

Young Modulus	Density	Spall strength	Length	Diameter
360 GPa	3840 kg/m^3	220 MPa	100mm	8mm

5.1. Reflection of the wave at the boundary

We begin by testing the behaviour of our model at the boundary. To do so, we consider a stress pulse of 450 MPa during 18μs. Here we do not consider any damage and we focus only on the duration and location of the reflected wave.

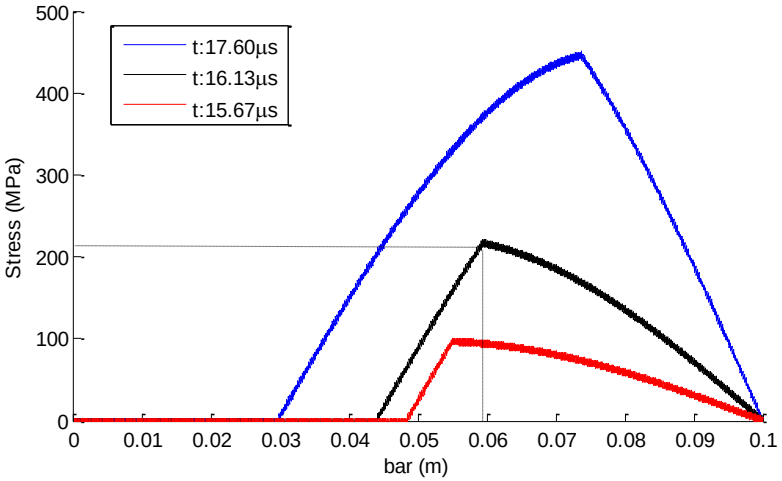

5.1- Rise of the tensile stress wave after reflection at the free surface

The results shown in figure 5.1 are in complete agreement with (Diaz, 2005).

On this first result we can already see the numerical noise that was mentioned in the stability of the model in section 4.4.

We continue by looking at the first result related to spalling, which will consist in the analysis of the velocity at the free-surface. This was said to be the main output of the plate-impact experiment as it is key to determine the spall strength of a material experimentally.

5.2. Free-surface velocity

As it was mentioned in the second chapter it is common to use the free-surface velocity of the sample to measure the dynamic fracture stress. As mentioned, a direct measurement of the peak surface velocity, u_0, and the free-surface velocity before spalling, u_m, allow us to calculate the tensile stress value just before spalling, i.e., the spall strength of the material. The formula given for the computation of this stress limit reads:

$$\sigma = \frac{1}{2}\rho_0 c_0 \Delta u_{fs}$$

where the velocity pullback, Δu_{fs}, was said to be the difference between u_0 and u_m. From experiments we see that the approximation is accurate if the density and the wave speed in the material remain close to their initial values, and as the tensile stress increases the relationship becomes less accurate. Using the mechanical parameters of table 5.1 and an impact load of 500 MPa we reach the surface velocity history given in 5.2.

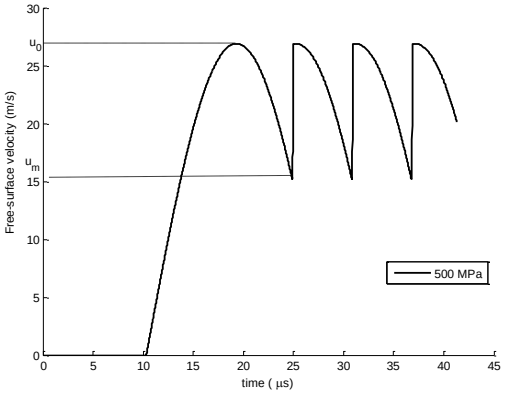

5.2 – Free-surface velocity for an impact load of 500MPa

A quick calculation using the values of the graph yields a value of 440MPa, in contrast to the 220MPa used as the stress threshold. It is important to notice that Δu_{fs} measures the strength of the material and it is independent of the applied load, so no connection should be made between the 440MPa and the impact load. Despite a clear discrepancy with the threshold value of 220MPa set in the model the value is consistent for different loads as shown in figure 5.3 for an impact load of 2141MPa.

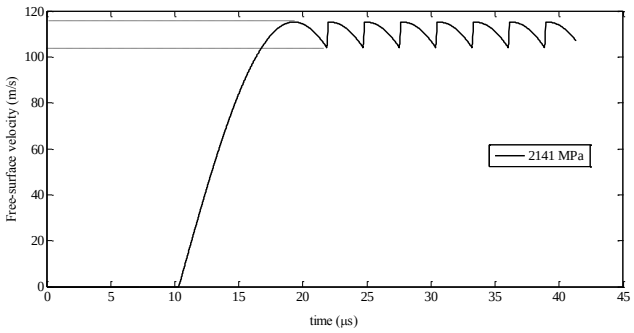

5.3 - Free-surface velocity for an impact load of 2141MPa

Leaving the spall strength aside we can analyse the pattern of the curve. In figure 5.3 we see that upon fracture, at the spall plane, the tensile stresses will quickly tend to zero and compression waves will form away from the plane. These waves will be trapped between the fracture location and the rear surface of the body, and the oscillations in the free-surface velocity are a reflection of this phenomenon.

The four models show a good agreement on the free-surface velocity prediction and hence in their first result on the ability to predict fracture for loads higher than the critical stress, as it can be seen in figure 5.4.

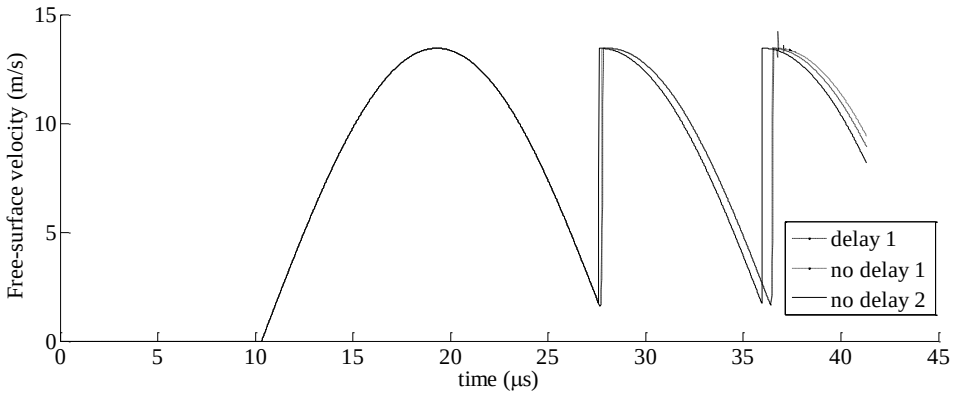

5.4 – Comparison of the free-surface velocity for a low impact test for three damage models.

Figure 5.5 below, shows the free-surface velocity for the Aluminum sample described above, for three different shock intensities. The lowest shock intensity is the curve of the delay mode 2 in figure 5.4. Here, we can see that the magnitude of the tensile stresses increases with increasing shock intensity, as predictable. As we can observe from this figure the particle velocity history has the same shape as the stress imposed initially up to fracture. Fracture then limits the wave to a section of the bar, as mentioned, causing the propagation of constant waves that fail to decrease in their intensity.

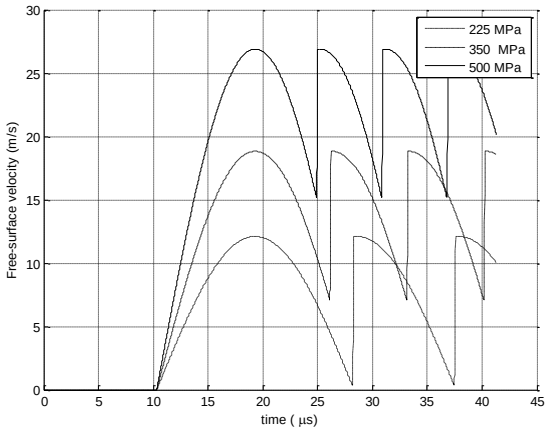

5.5 –Free-surface velocities for different impact loads

5.3. Measurement of spalled zone

The size of the spalled region is another equally important solution we seek from a numerical model. In this case we shall not analyse the spall strength of the material but look at the variation of the size of the spalled layer for different impact loads. Such measurement is shown in figure 2.2 for an aluminum sample. As this result involves clearly the behaviour of the damage model, in contrast to the results from the previous section, we shall begin by look at the response of each model for the damage profile at two loads.

The damage profiles for models 1-4 are shown sequentially from left to right, for two different impact shocks leading to stress waves of magnitudes 222 and 600 MPa, with a spall threshold of 220 MPa.

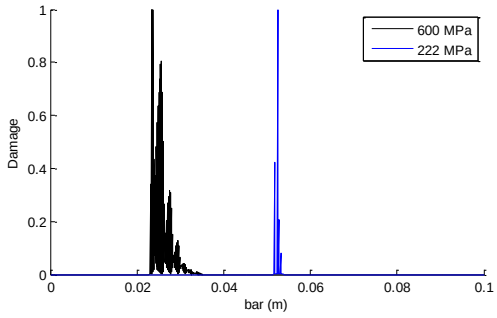

(a) No delay 1

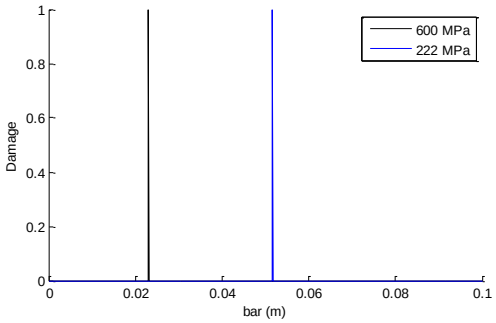

(b) No delay 2

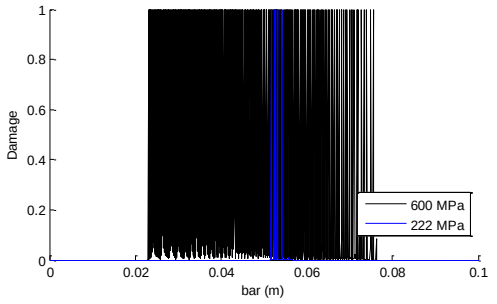

(c) Delay 1

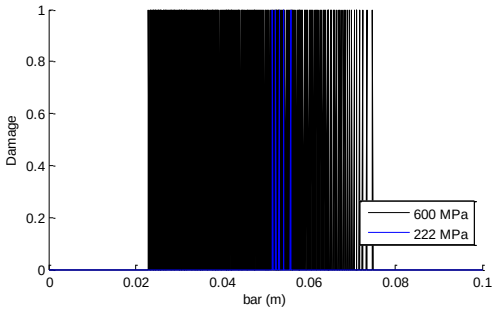

(d) Delay 2

5.6- Damage profiles for the four models

The computation time was set to guarantee the complete reflection of the stress wave one time.

The results show that the classical models present spurious localization. It was mentioned in chapter 3 that these models suffer from mesh dependency conditioning the fracture to a single element, and this result proves the phenomenon.

The damage profiles also show some numerical noise especially in the case of the delay models where we can see non-damaged elements in the vicinity of fractured elements for the low impact. This result is the proof of the suspicions raised in section 4.4. We mentioned the difficulties of the explicit schemes in dealing with strong discontinuities in the traction boundary conditions and the absence of damage in these elements shows the inability of the scheme to determine accurately the stresses in every element without oscillations.

From figure 5.6 we can see that the four models show a good agreement on the appearance of the spall plane.

Regarding the classical models we see that the first model shows a slower damage response registering damage in the sample over some extension as opposed to the second model, which simple shows damage over one element as soon as the spall limit is reached. We zoom in on the mesh to observe what is the actual shape of these peaks.

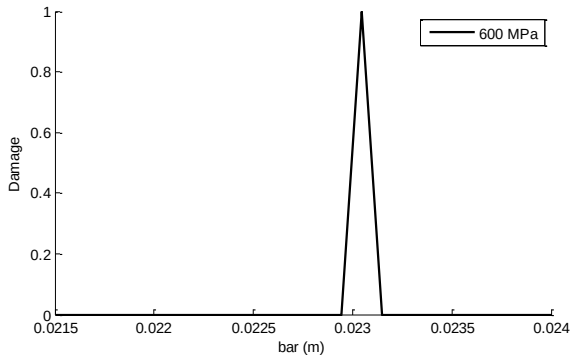

5.7 – Damage profile for the second model.

The damage profile for the case of model 2 shows the exact response we predicted in chapter 3 for this model. Damage grows linearly up to fracture, and we notice once more that fracture is conditioned to a single element

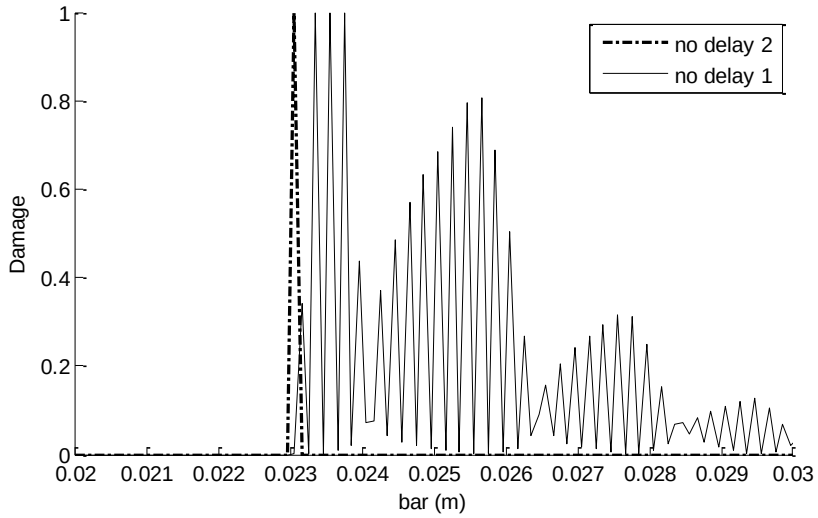

5.8 – Damage profiles for the no delay models impacted with a 600 MPa load.

The first model shows clearly a larger damaged zone, as damage initiation if directly dependent of the spall strength. The numerical oscillations lead to damage at stresses close to the critical value.

Considering now the case of the second delay model (model 4), we observe that the model is not predicting damage sequentially in the elements when we zoom in to a damaged point in a bar.

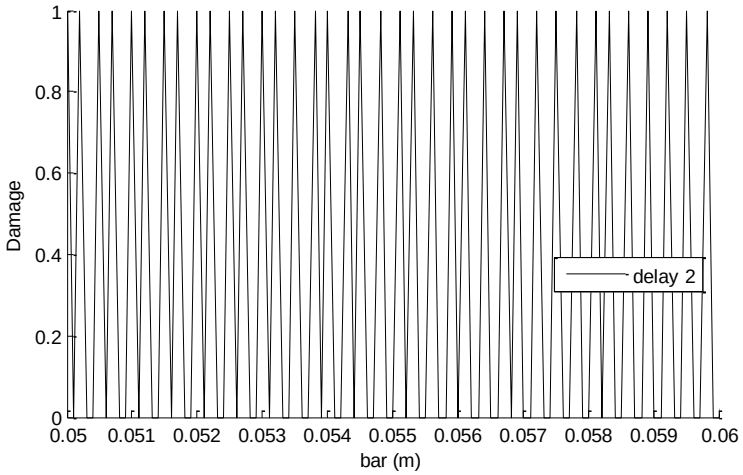

5.9 – Damage profile for model 4 for an impact load of 600 MPa.

This result shows that the fourth delay model will also guide damage to evolve linearly, but in contrast with the second delay model, it will be over a characteristic length. The fact that we are unable to represent the correct damage profile, that is d=1 over the fracture length lies in the inability of our explicit scheme to correctly account for external forces. Consequently, we consider the size of the damaged zone for the delay models as the difference between the first damaged element at the left and the last damage element at the right.

The actual determination of the size of the fracture zone is presented next. In figure 5.10 we see the response of the four models to varying loads for.

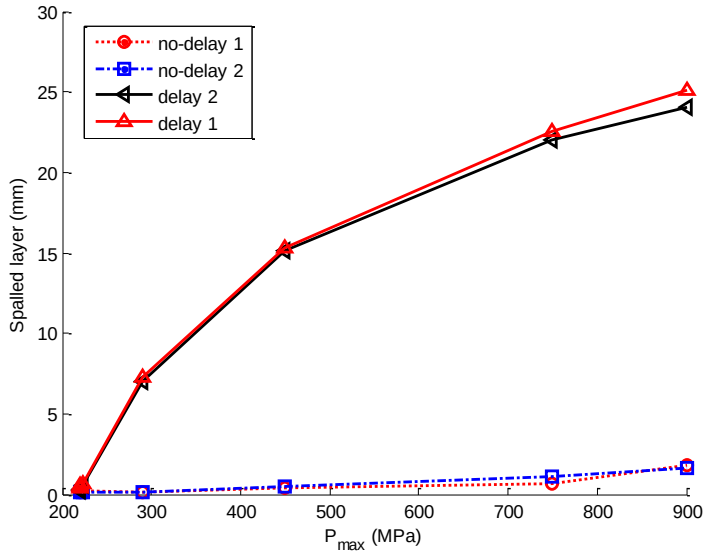

5.10-Size of the fractured zone for varying loads

The delay models show the pattern observed in figure 2.2 for the aluminum sample. However, neither the mechanical properties are the same nor the impact load.

Again, we can observe the lack of ability to capture the fractured zone for the classical models, as the size of the fractured zone does not increase with the impact load showing clear spurious localization. When we zoom in to see what happens at loads close to crack initiation we can make some conclusions.

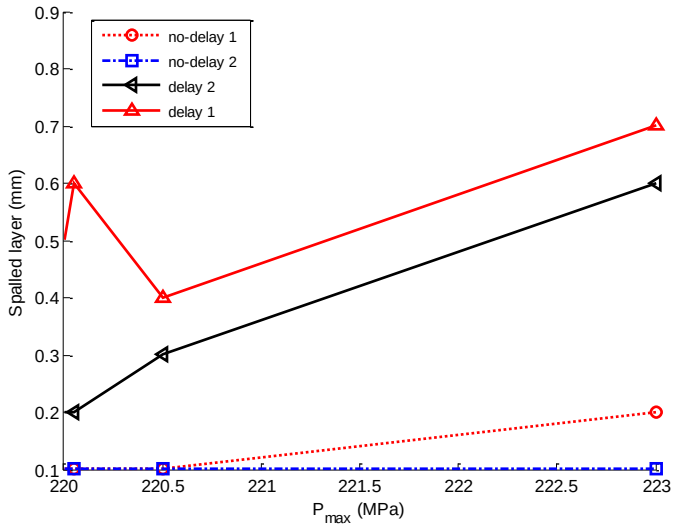

5.11 – Size of fractured zone for low impact

The first delay model shows an increase of the spalled layer with the increase stress but we have seen that it was a consequence of numerical noise and the fact that this damage model depends only on one parameter to initiate damage.

The second delay model show the classic case of mesh dependency, reducing damage to a single element.

The third model shows a total inability to predict the size of the spalled layer for low impacts and we justify it again by the dependency on only one parameter to predict damage initiation. Hence, for stresses close the threshold the parameters of this model are insufficient to describe a regular response, as it had been predicted in chapter 3.

The fourth damage model is the only one that is able to reproduce a physical relationship between the charging and the fractured zone.

The two delay models are depicteg again in figure 5.12 for an extremely fine mesh.

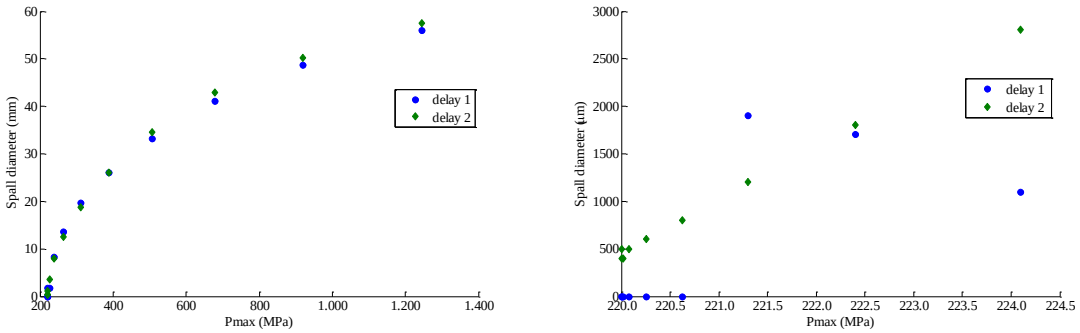

5.12- Spalled zone for varying loads, models 3 and 4.

As it was explained in chapter three the energy release function for the third delay model is clearly dependent on the time increment of the numerical time integration algorithm. As it is lower than τ_c in the case presented above, the model fails to simulate fracture for stress waves slightly over the stress limit.

5.4. Energy dissipation

The prediction of the energy dissipation upon fraction is another very important result in damage modeling. We defined the energy dissipation in chapter three and explained it is usually a difficult parameter to model in crack initiation.

The results for the energy dissipation for varying loads are present below:

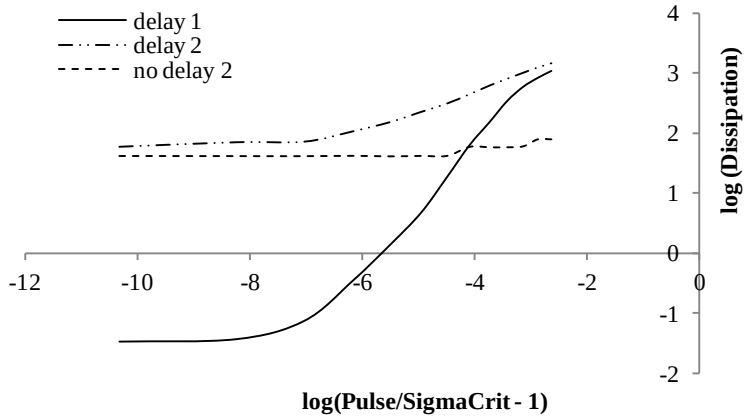

5.13 – Energy dissipation versus the impulse load applied for three models.

In the previous section we proved that the classical models suffer from spurious localization. These models will thus predict a constant dissipation as they limit damage to a small region of the bar. Hence the study of the variation of energy dissipation proves unnecessary in such cases.

Below, in figure 5.14 we show a relationship between the sizes of the spalled zone with the energy dissipation for low loads and very fine meshes.

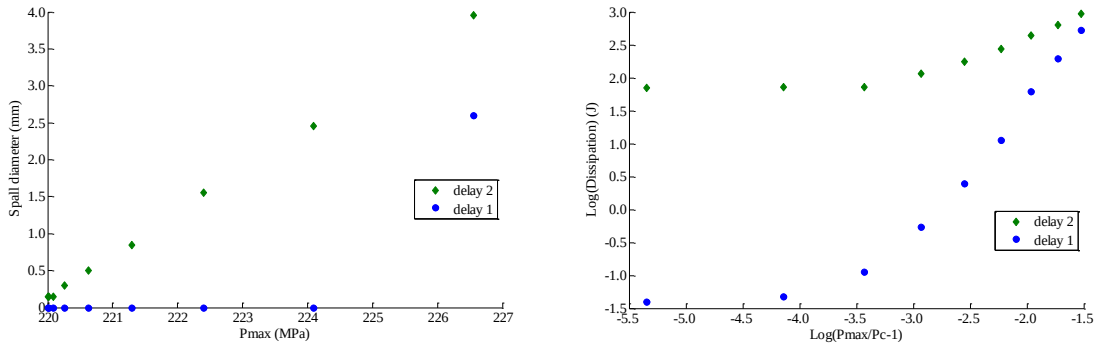

5.14- Comparison between the spallation zone and dissipated energy for the two delay models

As we can see above, the delay models show an inaccurate measure of the dissipation. This term seems to vanish in both cases when considering loads very close to the threshold. The graphs show the inability of the models to deal with the initiation of fracture.

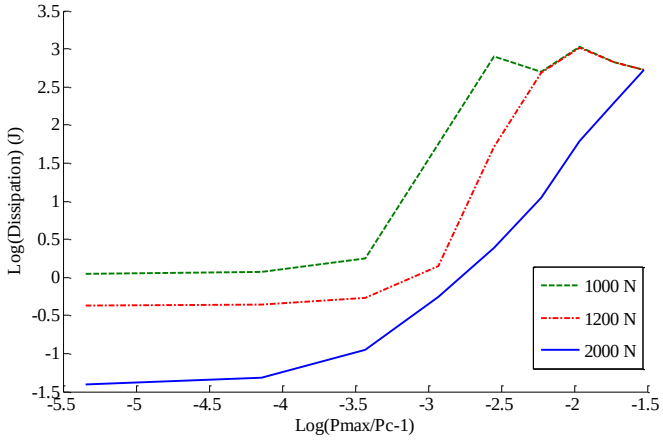

5.15 –Variation of the energy dissipation for model 3 using different mesh sizes.

The tendency seems to accentuate with the refinement of the mesh size as we see in figure 5.15 for the case of model 3. The variation of the mesh size and the pulse load with the energy dissipation is presented below for the two delay models.

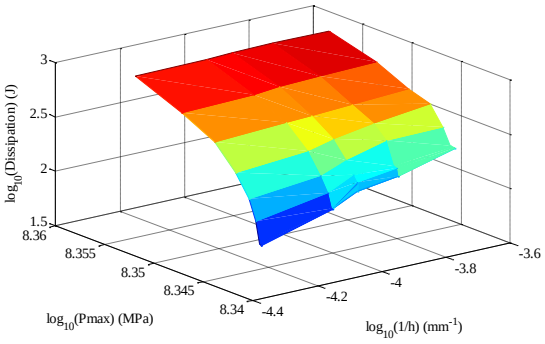

5.16 – Delay model 2

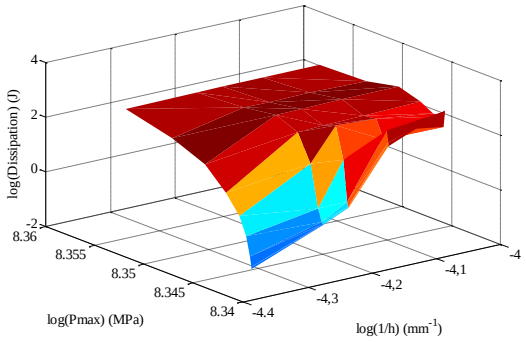

5.17-Delay model 1

As we can see above, delay model two is smoother in its response than the first model. However, it also misses the dissipation of energy upon fracture.

6. Conclusions

In this study we have implemented a numerical model based on the finite element method to simulate the dynamic fracture process of spalling. In order to do so, we have implemented four damage models and analyzed the response of each one according to the ability to identify the location of fracture and their prediction of the size of the spalled layer.

The investigation of spalling focus mainly in the determination of whether nucleation and damage growth occur inside the material due to stress wave propagation. Hence, an important result is the observation of the evolution of the micro-crack diameter with respect to the loads applied above a spall strength. This result is extremely interesting physically as it essays to establish a bridge between the continuum mechanics framework, used to model the average behaviour of a relevant volume element (RVE) of our material sample, with the experimental results that trace back to the molecular level of the material, such as the in (Rességuier, 2009,2010a and 2010b). The aim of this study was not to obtain such length scales but to identify a spalled region for a given test case.

We began by studying the free-surface velocity parameter, mentioning the importance of the velocity pull-back to measure the spall strength of a material. The results obtained for this variable lead to the calculation of a spall strength which was about twice the critical value assumed in the models. In contrast, it showed a pattern in accordance to the experiments, describing a wave travelling between the spall plane and the rear surface of the sample after fraction. This prediction was common for all four models. Lastly, the wave generated after spalling did not decay in intensity as damage dynamics were not considered.

When observing applied loads very close to the value of the threshold we are before crack initiation. As referenced in (Allix, 2002) damage mechanics requires the gradual loss of stiffness in an extremely small area, and modelling damage thus demands special care to avoid spurious localization. In the other two models presented, a length scale was introduced, to avoid this disorder.

The first two models presented were purely local classical models. Their implementation had the objective of proving their inability to describe the physics of the phenomenon. These models proved to be inadequate because of their well-known mesh dependency, leading to spurious localization.

The third model proved to be completely inaccurate for values in the vicinity to the threshold, as the numeric method associates the material variables to the time increment yielding damage for loads under the critical value when the time increment of the time integration algorithm is smaller than the parameter τ_c and it does not predict fracture for loads just above the critical

stress when the time increment of the time integration greater than the parameter. Its dependence on only one critical parameter to determine the energy release function completely conditions its behaviour.

The fourth damage model is the only one that is able to reproduce a physical relationship between the charging and the fractured zone.

The analysis of the energy dissipation was reserved to the delay models, due to the fact that the mesh dependency of the classical models predicted a constant fracture size for fine meshes, completely disregarding the magnitude of the pulse of the stress wave. In the delay models we see a clear tendency for the dissipated energy to vanish for loads close to the threshold, a tendency which is accentuated by the mesh refinement. From here we conclude that not even our last model can physically describe our fragmentation process.

References

ALLIX, O. and DEÜ, J. (1997). Delayed-damage modelling for fracture prediction of laminated composites under dynamic loadin. *Engineering Transactions*. 45 (1), pp 29-46.

ALLIX,O. and HILD, F. (2002). *Continuum Damage Mechanics of Materials and Structures*, New York, ELSEVIER.

ANTOUN, T, et al. (2002), *Spall Fracture*, New York, Springer.

BATHE, K. (1996). *Finite Element Procedures*, New Jersey, Bathe, K.

BELYTSCHKO, T. (2000). *Finite Elements for Nonlinear Continua & Structures*, Northwestern, BELYTSCHKO, T.

BONET, J. and WOOD, R. (1997). *Nonlinear Continuum Mechanics for Finite Element Analysis*, Cambridge, Cambridge University Press.

DIAZ, F. PEREZ, J and GALVEZ, V, (2002). The spalling of long bars as a reliable of measuring the dynamic tensile strength of ceramics. *International Journal of Impact Engineering*, 27, pp 161-177.

HOLZAPFEL, G.A. (2000). *Nonlinear Solid Mechanics*, West Sussex, John Wiley & Sons Ltd.

KOLSKY, H. (1963). *Stress Waves in Solids*, New York, Dover Publications

LEMAITRE, J. (1996). *A Course in Damage Mechanics*, Paris, Springer.

LEMAITRE, J. and DESMORAT, R. (2004). *Engineering Damage Mechanics*, New York, Springer.

RESSÉGUIER, T. et al., (2010). Dynamic fragmentation of laser Shock-melted tin: experiment and modeling.*Int J Fract,* 163, pp 109-119.

RESSÉGUIER, T. et al., (2010a). Wave Propagation and Dynamic Fracture in Laser Shock- Loaded Solid Materials.*Wave Propagation in Materials for Modern Applications,* p 526.

RESSÉGUIER, T. et al., (2010b). Dynamic Fragmentation of Laser Shock-Melted Metals: some experimental advance. *Journal of Theoretical and Applied Mechanics*, 48 (4), pp 957-972.

SHORR, B.F. (2004). *The Wave Finite Element Method*, Berlin, Springer.

STRAUSS, W., (2008). Partial differential equations – An introduction, United States of America, John Wiley & Sons Ltd.

SUFFIS, A. et al., (2003). Damage model with delay effect, Analytical and numerical of the evolution of the characteristics damage length-annotated. *International Journal of Solids and Structures*, 40, pp 3463-3476.